Available online at www.sciencedirect.com

ScienceDirect

Journal of Colloid and Interface Science 306 (2007) 262–273

JOURNAL OF Colloid and Interface Science

www.elsevier.com/locate/jcis

Turbulent hydrodynamic stress induced dispersion and fragmentation of nanoscale agglomerates

R. Wengeler, H. Nirschl *

Institute for Mechanical Process Engineering and Mechanics, Universität Karlsruhe (TH), D-76128 Karlsruhe, Germany

Received 28 July 2006; accepted 25 October 2006

Available online 28 October 2006

Abstract

High pressure dispersion nozzles of 2.5–10 mm length and 125 μm diameter have been characterized in terms of fluid dynamics and dispersion experiments at 100–1400 bar. Elongational stresses at the nozzle entry (5×10^5 Pa) and turbulent stresses up to 10^5 Pa at a Reynolds number of 25,000 in turbulent channel flow are identified crucial for desagglomeration and aggregate fragmentation. Maximum stresses are calculated on representative particle tracks and related to agglomerate breakage. Agglomerates in the experimental study are in the range of the Kolmogorov micro scale (100–400 nm) and therefore break due to turbulent energy dissipation in viscous flow. Bond strength distributions could be determined experimentally from particle size distributions and fluid dynamics simulations, with primary particle erosion determined as dispersion mechanism for diffusion flame silica particles. Nanoscale agglomerates show a power law scaling for breakage with scaling exponents diverging from theory of floc dispersion. This is attributed to their strong bonding by sinter necks.

Keywords: Dispersion; Turbulent flow; Hydrodynamic stress; Nanoparticles

1. Introduction

Nanoparticles constitute the disperse phase in nanocomposites improving optical, mechanical, thermal or handling properties, i.e., for UV protection [1] or translucency of dental materials [2]. Inorganic nanoparticles are synthesized mainly by flame technology [3] which leads to agglomerated powders (e.g., fumed silica and titania). Particles are agglomerated physically by van der Waals forces as agglomerates, or by stronger chemical or sintering bonds [4] as aggregates. The degree of agglomeration strongly affects material performance and depends on synthesis process conditions [5]. For nanoscale particles van der Waals and sintering bond forces are very high [6].

Compounding requires re-dispersion of dry particles in an aqueous or monomer solution [7,8]. Therefore liquid dispersion of agglomerates is required for material processing with exertion of high stresses on the constituent particles. Rheometrical flow conditions fail to impose such stresses on aqueous suspensions. Hence stresses are commonly applied by agitated ball mills [9] and ultrasonic [10,11] or high pressure dispersion systems. Here, a high pressure dispersion apparatus for abrasive dispersions [12] is used to exert very high stresses on particles to break up physical bonds as well as weak sinter necks. It provides reproducibly stable suspensions, where perikinetic re-agglomeration by attractive inter-particle forces is eliminated.

Different dispersion geometries have been reported for high pressure dispersion and homogenization [13]. These induce strong hydrodynamic stresses in turbulent fluid flow due to pressure drops of 800–2500 bar and high Reynolds numbers of 15,000–50,000 [12]. Axial elongational stresses at the dispersion channel entrance have been related to droplet break-up [14]; whereas Zumaeta et al. [15] related agglomerate break-up to the turbulent energy dissipation rate. Yet, a thorough analysis including a breakage model for fractal nanoscale agglomerates and comparing laminar and turbulent hydrodynamic stresses in high pressure dispersion has not been presented in literature.

This study describes the flow field and hydrodynamic stresses within a dispersion nozzle calculated by computational fluid dynamics (CFD) and validated with experimental data. It correlates pyrogenic, nanoscale agglomerate fragmentation

* Corresponding author. Fax: +49 721 608 2405.
E-mail address: hermann.nirschl@mvm.uni-karlsruhe.de (H. Nirschl).

0021-9797/$ – see front matter
doi:10.1016/j.jcis.2006.10.065

to a new break-up criterion reflecting hydrodynamic stresses and agglomerate strength. Agglomerate elasticity and critical strength are evaluated. Experimental and theoretical data of agglomerate break-up on the nanoscale are compared to macroscale conditions.

2. Theoretical approach

2.1. Fluid dynamics

Turbulent flows are described by decomposing the velocity U_i into its mean $\langle U_i\rangle$, where rectangular brackets indicate time averaging, and the fluctuation u_i. This is referred to as Reynolds decomposition $U_i = \langle U_i\rangle + u_i$. From applying this decomposition to the Navier–Stokes equations follows a mean momentum equation or Reynolds equation [16].

$$\rho_f \frac{D\langle U_i\rangle}{Dt} = \frac{\partial}{\partial x_i}\left[\nu\rho_f\left(\frac{\partial\langle U_i\rangle}{\partial x_j} + \frac{\partial\langle U_j\rangle}{\partial x_i}\right) - \langle p\rangle\delta_{ij} - \rho_f\langle u_i u_j\rangle\right] \quad (1)$$

with ρ_f fluid density, ν kinematic viscosity, p static pressure and δ_{ij} Kronecker delta. Here, momentum is transformed into three stress components which are consequently described in detail: viscous stresses, isotropic stress due to pressure differences and Reynolds stresses arising from turbulent velocity fluctuations. Viscous and Reynolds stresses are characterized by kinetic energy dissipation. On small scales Reynolds stresses dissipate in thermal energy. The total dissipation rate in kinematic form [17] is given by

$$E + \varepsilon = \frac{1}{2}\nu\left[\left(\frac{\partial\langle U_i\rangle}{\partial x_j} + \frac{\partial\langle U_j\rangle}{\partial x_i}\right)^2 + \left\langle\left(\frac{\partial u_i}{\partial x_j} + \frac{\partial u_j}{\partial x_i}\right)^2\right\rangle\right], \quad (2)$$

which is the mass specific energy. It decomposes analogously to Reynolds decomposition of velocities into a first part $E = 1/2\nu(\partial\langle U_i\rangle/\partial x_j + \partial\langle U_j\rangle/\partial x_i)^2$ describing dissipation rate of kinetic energy E with the shear rate

$$\dot\gamma_l = \sqrt{E/\nu} \quad (3)$$

being a cumulative measure for the mean velocity gradients $\dot\gamma_l$. The second part is the mean turbulent energy dissipation rate ε corresponding to a turbulent velocity gradient $\dot\gamma_t$ defined analogously

$$\dot\gamma_t = \sqrt{\varepsilon/\nu}. \quad (4)$$

The corresponding stresses are readily deduced as $\tau = \nu\rho_f\cdot\dot\gamma$. On the scale of large eddies, inertial energy convection is responsible for agglomerate break-up by turbulent Reynolds stresses, whereas smallest eddies dissipate their energy in viscous motion [18,19]. Stresses on structures of this smallest eddies' length scale, the Kolmogorov's micro scale,

$$\eta = \left(\nu^3/\varepsilon\right)^{1/4}, \quad (5)$$

can be modeled by viscous shear [20]. Kolmogorov's first similarity hypothesis states that relative velocity differences v_d are uniquely determined by fluid viscosity and turbulent energy dissipation rate provided that the length scale is small compared to the macroscale. Using a structure function describing turbulent flow statistics v_d are described by

$$v_d^2 \approx (\varepsilon\nu)^{1/2}\beta_2. \quad (6)$$

The universal, second order function β_2 for the statistics on the microscale is defined as $\beta_2 = 1/15\cdot(d/\eta)^2$ for $d < \eta$ [19], d being a characteristic length scale. But it is valid with deviations below 5% for $0 \leqslant d/\eta \leqslant 3.5$ [21].

Stresses passed from turbulent flow to agglomerates are transduced by shear stress from fluid flow, particle–particle and particle–wall collisions. Here, collisions are negligible because of very low volume concentrations of 0.001 v/v. Turbulent flow places a permanent, fluctuating stress on the agglomerates. Yet, for small structures stresses are transduced by laminar shear. Taylor [22,23] studied a rotating sphere in laminar flow. Normal stresses on the surface of a particle in laminar flow are

$$\tau_N = k\cdot\nu\rho_f\cdot\dot\gamma_l \quad (7)$$

with $k = 2.5$ [22]. Secondly surface shear can be considered with stresses τ_S which are equal to normal stresses $\tau_N = \tau_S$ shown at low Reynolds numbers by Taylor [23] and extended to medium Reynolds numbers (1–100) by Nirschl [24]. Here, correspondingly turbulent stresses are characterized by $\tau = k\cdot\nu\rho_f\cdot\dot\gamma_t = k\cdot\rho_f v_d^2$ using Eqs. (4) and (6).

2.2. Agglomerate strength

Agglomerate dispersion can be achieved by two limiting mechanisms, agglomerate break-up and erosion. Agglomerate tensile strength as a limiting condition for break-up often is modeled based on the concept of Rumpf [25]

$$\sigma_{Agg,B} = \frac{F_B}{d_P^2}S \quad \text{with } S = \frac{1-\varphi}{\varphi}. \quad (8)$$

He relates agglomerate strength σ_{Agg} to the bond force F_B and a structural model S associated with the agglomerate porosity φ assuming a constant φ throughout the agglomerates. Erosion of agglomerates can be modeled by a virtual surface tension $\phi = F_B/d_P\cdot S$ [26], which results in the yield strength

$$\sigma_{Agg,E} = \phi/d_{Agg}. \quad (9)$$

The floc porosity function S is related to the fractal dimension [27] by

$$\frac{1-\varphi}{\varphi} = A(d_{Agg}/d_P)^{d_f-3} \quad (10)$$

with $A \sim 1$ [28] for large agglomerates. Russel and Sonntag [29,30] defined σ_{Agg} by assuming a power law function of φ using a simpler porosity function $S_1 = 1-\varphi$ and introducing a parameter r as

$$\sigma_{Agg} = \sigma_0 S_1^r. \quad (11)$$

For $r = 1$, σ_0 is related to the bond force $\sigma_0 = F_B/d_P^2$ as in Eq. (8), while for $r \neq 1$ this is not true [21]. The parameter

r results from solid mechanics assumptions considering agglomerates as an elastic network and represents the 'elastic' properties. For elastic agglomerates $r \leqslant 1$, while r increases with inelasticity for non-deformable agglomerates with strong bonding.

Agglomerates break up when hydrodynamic stresses exceed agglomerate strength. Rheological studies interpret these stresses as volume specific energy [11,31] whereas others consider a fragmentation number Fa defined as $\nu\rho_f \cdot \dot{\gamma} = \mathrm{Fa}\,\sigma$ and determine a critical, local Fa for breakage [32–34]. Breakage models for agglomerates based on hydrodynamic stresses relate experimental [29,35] as well as simulation data [36,37] of agglomerate diameters depending on shear rate in the form

$$d_{\mathrm{Agg}} = C \cdot \dot{\gamma}^{m}, \tag{12}$$

where C and m are empirical parameters. Parker et al. [38] made an attempt to define these parameters through theory. Mason [35] characterized physico-chemical influences on C and m, which are especially important for small particles. Recently, Bache [21] derived such an expression for fractal agglomerates using an energy balance formulating hydrodynamic stresses by Eq. (4) and agglomerate strength based on a modification of Eq. (8). Thus, agglomerate breakage in turbulent flow fields can be explained with a breakage criterion based on (i) a hydrodynamic stress model and (ii) a model of agglomerate breakage (distinguishing break-up and erosion), structure and bond strength.

3. Numerical method

An axis symmetrical, 2D geometry represents the experimental, high pressure dispersion nozzle. The relevant geometry includes the entrance section, a dispersion channel section and a turbulent jet into the exit section. The geometry is set up as shown in Fig. 1 with section lengths $l_c = 2.5, 5, 7.5$ and 10 mm, $l_{\mathrm{entry}} = 2$ mm, $l_{\mathrm{exit}} = 10$ mm, and diameters $d_c = 125$ µm and $d_{\mathrm{entry}} = d_{\mathrm{exit}} = 2$ mm.

A structured mesh is refined in the boundary areas of high stresses and pressure drops consisting of more than 200,000 nodes. On the radius of the capillary originally 60 cells have been distributed equidistantly. Inside the first two cell layers additional six cell layers were defined for boundary layer resolution. Boundary layer refinement led to a wall Y^+-values below 1.0 (with a maximum of 1.8 at the sharp edge at the channel entrance) enabling to use a two layer zonal model for wall treatment resolving the viscous sublayer.

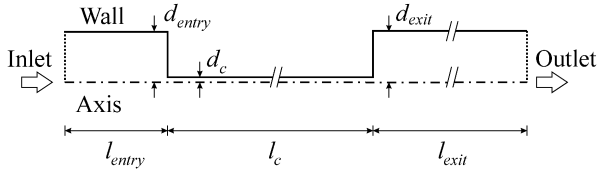

Fig. 1. Axis symmetric, 2D geometry for CFD calculations representing the dispersion nozzle. Boundary faces for inlet, outlet, axis and wall, as well as physical dimensions for the lengths l and diameters d of the three sections *entry*, channel c and *exit*, are indicated.

The boundary conditions are set as no slip boundary condition for all walls. The inlet defines the channel Reynolds number by fixing the inlet velocity and the outlet is defined as equal to ambient pressure. The central axis is defined as symmetry axis. An axis symmetrical, implicit, incompressible solver (FLUENT Inc. 6.2.16) is used for calculations based on a second order spatial discretization of all variables and pressure-velocity coupling using a SIMPLE scheme. The Navier–Stokes equations are extended for turbulence modeling using the k–ε-model [39] with a realizable scheme proposed by Shih et al. [40]. The constituting equations are given for the turbulent energy k and the turbulent energy dissipation rate ε. Turbulent energy is balanced by transport, production and dissipation with ε evoking stresses on small scale structures as characterized in this study.

Convergence and solution behavior are monitored by the use of normalized residuals for each equation. All residuals attain values below 10^{-8} indicating a converged solution. The sensitivity of the solution has been checked showing no influence of grid refining. The pressure drops of the dispersion channel have been validated by comparison to Blasius resistance formula (Eq. (13)) for turbulent channel flows [16]:

$$\lambda = 0.3614 \cdot \mathrm{Re}^{-0.25}. \tag{13}$$

A good correlation of the numerical results was observed $(\Delta p_{\mathrm{Blasius}} - \Delta p_{\mathrm{CFD,c}})/\Delta p_{\mathrm{Blasius}} < 2\%$. Also, the pressure drop across the geometry was validated with experimental results and confirmed by published data as will be shown in Section 5.

4. Experimental method and materials

4.1. High pressure dispersion

Flame-synthesized, nanoscale particles (0.001 v/v) were stirred into distilled water and stabilized by 0.1 mM $Na_4P_2O_7$. The aqueous suspensions were passed through a high pressure dispersion apparatus (Fig. 2). The high pressure is generated by a pneumatic–hydraulic pressure intensifier (DU 3440 by Maximator, Germany), which transforms pneumatic pressures in the range of 0 to 10 bar by a ratio of 1:185 with a maximum hydraulic pressure applied of 1500 bar. From the reservoir a sample of 70 ml suspension is delivered to the high pressure

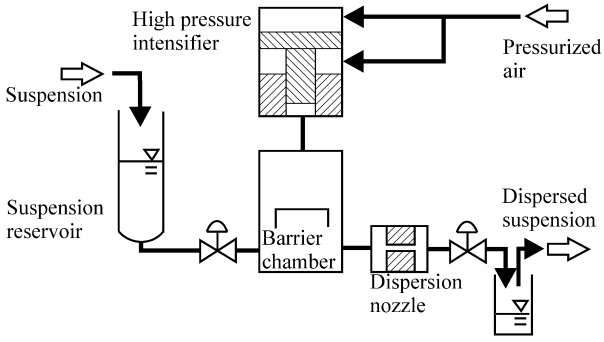

Fig. 2. High pressure dispersion apparatus: The suspension from the reservoir passes a barrier chamber and through the dispersion nozzle with a pressure drop of up to 1500 bars where suspended particles are fragmented upon expansion.

section and compressed by applying high pressure. A pressure drop ranging from 200 to 1400 bar was applied by the high pressure intensifier that was fueled by pressurized air. As the piston moves down the suspension was pressed through ceramic nozzles with a dispersion channel diameter of 125 μm and 2.5, 5, 7.5 and 10 mm length. The dispersed suspension was collected in a second container for particle size analysis.

4.2. Particle and dispersion characterization

Specific surface area of the powders and their suspension are measured by nitrogen adsorption (BET) and small angle X-ray scattering (SAXS) with identical results of the two methods. Also, fractal structure and other parameter were measured using SAXS. Data treatment and evaluation from the SAXS pattern measured at the European Synchrotron Radiation Facility (high brilliance beamline ID 02; Grenoble, France) is described in detail elsewhere [41].

Zeta potential measurements on the surface potential of the particles were performed with a Pen Kem 501 (Collotec Messtechnik GmbH, Germany). Agglomerate diameters in suspension were determined by dynamic light scattering (DLS; N4 Plus, Beckmann Coulter). An autocorrelation function of the resulting fluctuations in the scattering intensity resolved the characteristic time scales of Brownian motion. These time scales correlate with the mean diffusion coefficient D from which a diffusion equivalent particle diameter (d_{DLS}) was calculated form the Stokes–Einstein equation as $d_{DLS} = (k_B T)/(3\pi \nu \rho_f D)$ with the Boltzmann constant k_B and temperature T. While a constrained regularization algorithm (CONTIN [42]) was used to resolve the agglomerate size distributions.

4.3. Nanoscale powders

Commercially available pyrogenic nanoscale silica powders have been used, namely Aerosil 200, 150, 90 and Ox50 by Degussa AG (Germany) as well as flame synthesized particles from a former study [12]. Table 1 shows the material properties of the particles studied by high pressure dispersion. The specific surface area (SSA) ranges from about 50 to 200 m^2/g for the Aerosil particles as well as silicas S2 to S10 from a co-flow diffusion flame (DF) reactor. Here, the numbers correspond to oxygen flow rates of 2 to 10 L/min, where increasing oxygen flow rates lead to smaller particles and a higher degree of agglomeration. The agglomerate diameter of the stirred-in sample is measured by DLS ranging from 278.6 to 396.1 nm for the 'Aerosil' samples, while S2 to S10 yield lower values at comparable SSA. Agglomerate diameters increase with decreasing SSA. The aggregation number Z_{Agg} is related to the radii of gyration R_g and displays the mean number of primary particles per agglomerate. It is calculated from SAXS [43] as

$$Z_{Agg} = \left(R_{g,Agg}^2 / R_{g,P}^2\right)^{d_f/2}. \quad (14)$$

Lower agglomerate sizes of the prepared silica samples S2 to S10 compared to Aerosil reflect in lower agglomeration numbers at 1400 bar. The mass fractal dimension d_f describing agglomerate structure varies only slightly within 2.1 and 2.2

Table 1
Material properties for the powders dispersed indicating specific surface area SSA determined by SAXS in liquid dispersion, agglomerate size before dispersion $d_{DLS,0bar}$ from DLS measurements, aggregation number (Eq. (11)) $Z_{Agg,SAXS}$ and the fractal dimension d_f, both from SAXS

Material	SSA (m^2/g)	$d_{DLS,\ 0bar}$ (nm)	$Z_{Agg,\ SAXS}$	D_f (–)
Aerosil 200	190.0	278.6	304.7	2.17
Aerosil 150	164.5	302.7	253.4	2.16
Aerosil 90	108.4	348.4	199.4	2.18
Aerosil Ox50	49.85	396.1	25.1	2.20
DF-silica S10	184.8	205.3	264.2	2.32
DF-silica S7	150.4	224.5	67.9	2.17
DF-silica S4	94.82	243.2	43.0	2.15
DF-silica S2	53.64	257.4	8.8	2.16

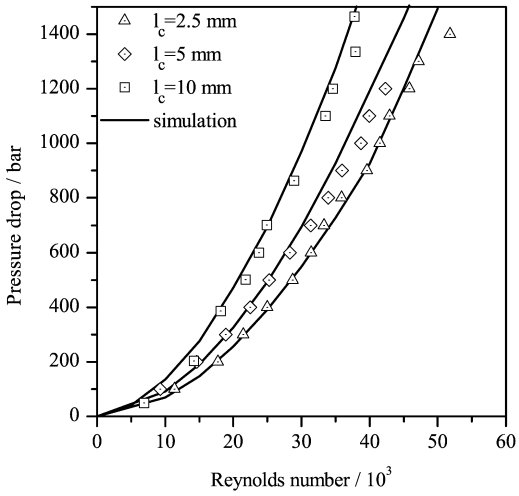

Fig. 3. Pressure drop plotted vs Reynolds numbers from experiments and from CFD calculations for capillaries of $l_c = 2.5, 5$ and 10 mm are in mutual agreement.

indicating a reaction limited cluster agglomeration [44]. An exception is S10 with higher values indicating a diffusion dominated agglomeration process [45]. d_f does not change by high pressure dispersion, due to sinter neck bonding [46] opposed to soft agglomerate processing studies [47,48]

5. Results and discussion

5.1. Flow field and hydrodynamic stresses

5.1.1. Flow field inside dispersion nozzle

The pressure drop across the geometry as well as the pressure drop due to turbulent channel flow inside the dispersion channel have been studied and compared to experimental data. These depend on Reynolds number and channel length. Fig. 3 shows a good agreement of the numerical pressure drops with experimental data (i.e. $\Delta p_{exp} = 695$ bar $\sim \Delta p_{num} = 680$ bar for $Re = 25{,}000$ at 10 mm).

Since experiments show an increase in suspension temperature of ~10 K at high dispersion pressure drops, calculations have been done at different suspension temperatures of 293, 303 and 313 K. Temperature increase results in a slight decrease in pressure drop of <5% from 293 to 303 K due to lower viscos-

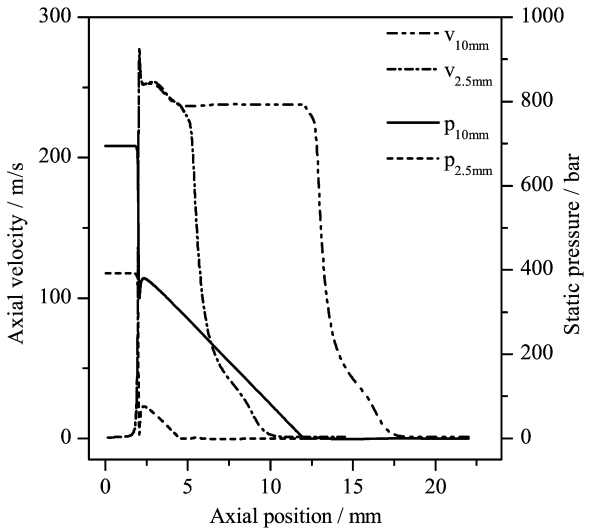

Fig. 4. Axial velocity and static pressure along centerline for $l_c = 2.5$ and 10 mm at Re = 25,000 reveal high stress domains at channel inlet, inside channel and in turbulent jet.

ity. Thus, for further calculations material data are defined for 293 K. Also, the sensitivity of the numerical results towards compressibility has been assessed. Adapting the physical properties of the liquid with the compressibility $\kappa = \Delta V/V \times \Delta p = 4.6 \cdot 10^{-10}$ Pa^{-1} of water at 293 K reduces the speed of convergence significantly, while the solution changes no more than 1% in the analyzed data for pressure drop, maximum stresses and turbulence energy dissipation. Therefore compressibility is neglected for all further calculations.

Fig. 4 shows the centerline profiles for static pressure and axial velocity at Re = 25,000 for $l_c = 2.5$ and 10 mm. Due to low entry section velocities no significant pressure drop is observed in this section. The abrupt contraction and velocity increase Δv leads to an entry pressure drop Δp_e which is related to the stagnation pressure $\Delta p_{stag} = (1/2)\rho_f \Delta v^2$. Resulting numerical $\Delta p_e/\Delta p_{stag} = 1.51$–$1.53$ are consistent with a loss coefficient of 1.5 at Re = 10,000 [49]. The entry pressure therefore depends only on the Reynolds number and is independent of the channel length. Afterwards the pressure decreases linearly with the dispersion channel length. The pressure drop of the turbulent jet is negligible ($\Delta p_{exit} = 1.9$ bar) compared to the total pressure drop of $\Delta p = 1000$ bar consistent with [16].

In the wide entry section the velocity is low (0.78 m/s and Re = 1562). The abrupt contraction to the dispersion channel results in a steep increase of the velocity which reaches a maximum value after the channel entrance due to the flow contraction [50]. Here, a contraction of $d_{entry}/d_c = 16$ where velocity profiles and corresponding stresses are insensitive to variations ($d_{entry}/d_c > 4$). The velocity profile develops yielding a mean axial velocity of 200 m/s at Re = 25,000 given by the Re applied. Even for a short dispersion channel of 2.5 mm complete development of the turbulent velocity profile and constant axial velocity are reached after a significant inflow region. Thus, the velocity profile of the turbulent jet is independent of channel length. At the end of the channel the velocity rapidly decreases due to widening of the turbulent jet.

The velocity and pressure profile along the axis identifies three regions which contribute to particle dispersion. The abrupt contraction with its sharp increase in velocity and decrease in pressure results in high macroscale elongation rates and a pressure gradient stress. High velocity and radial velocity gradients inside the turbulent channel lead to high turbulent energy dissipations rates and a macroscale shear deformation. The turbulent jet with a rapid velocity decrease yield elongational and turbulent energy dissipation.

5.1.2. Characterization of hydrodynamic stresses

Hydrodynamic stresses along particle tracks have been analysed by Euler–Lagrange particle tracking. Stokes numbers being the quotient of particle response time scale τ_v to flow time scale τ_F [51] for nanoscale agglomerates of $d_{Agg} = 200$ nm at Re = 25,000 are

$$\mathrm{St} = \frac{\tau_V}{\tau_F} = \frac{\rho_P d_{Agg}}{18\nu\rho_f} \cdot \frac{v_d}{d_C} = 3.5 \times 10^{-3}. \tag{15}$$

Thus particle have ample time to respond on flow field fluctuations (St < 1) and particle tracks resemble fluid path lines. Due to low Stokes numbers and low particle volume concentration one way coupling for particle tracking suffices. As identified in the last section the following hydrodynamic stresses are calculated with $d_{Agg} = 200$ nm as reference value and $(u_{p,xi}, u_{p,xj})^T$ being the particle velocity vector:

- Elongational stress parallel to particle motion:

$$\tau_e = \nu\rho_f \sqrt{\left(\frac{\mathrm{d}U_{xi}}{\mathrm{d}x_i} u_{p,xi}\right)^2 + \left(\frac{\mathrm{d}U_{xj}}{\mathrm{d}x_j} u_{p,xj}\right)^2}. \tag{16}$$

- Shear stress orthogonal to particle motion:

$$\tau_s = \nu\rho_f \sqrt{\left(\frac{\mathrm{d}U_{xi}}{\mathrm{d}x_j} u_{p,xi}\right)^2 + \left(\frac{\mathrm{d}U_{xj}}{\mathrm{d}x_i} u_{p,xj}\right)^2}. \tag{17}$$

- Turbulent stress:

$$\tau_t = \rho_f(\varepsilon \cdot \nu)^{1/2} \cdot \frac{1}{15}\left(\frac{d_{Agg}}{\eta}\right)^2. \tag{18}$$

- Compressive stress:

$$\tau_c = \Delta p_{max}/\Delta x \cdot d_{Agg}. \tag{19}$$

Fig. 5a shows these stresses (Eqs. (16)–(19)) along the centerline, where shear stresses (Eq. (17)) are zero. Within the entrance region, pressure gradient, shear and elongational stresses reach their maximum. The figure inlet expands the entrance region and shows maximum compressive and elongational stresses, which rapidly decay after the contraction. The width and magnitude of maximum stresses at the channel entrance depend on the entry geometry as shown for the strain rate by [14]. For smoother geometries the peak gets wider and its maximum value decreases. In the entry region no turbulent stresses occur in laminar flow. These reach a first maximum shortly after the entrance and laminar–turbulent flow transition as observed also by Zumaeta et al. [15]; and they increase to

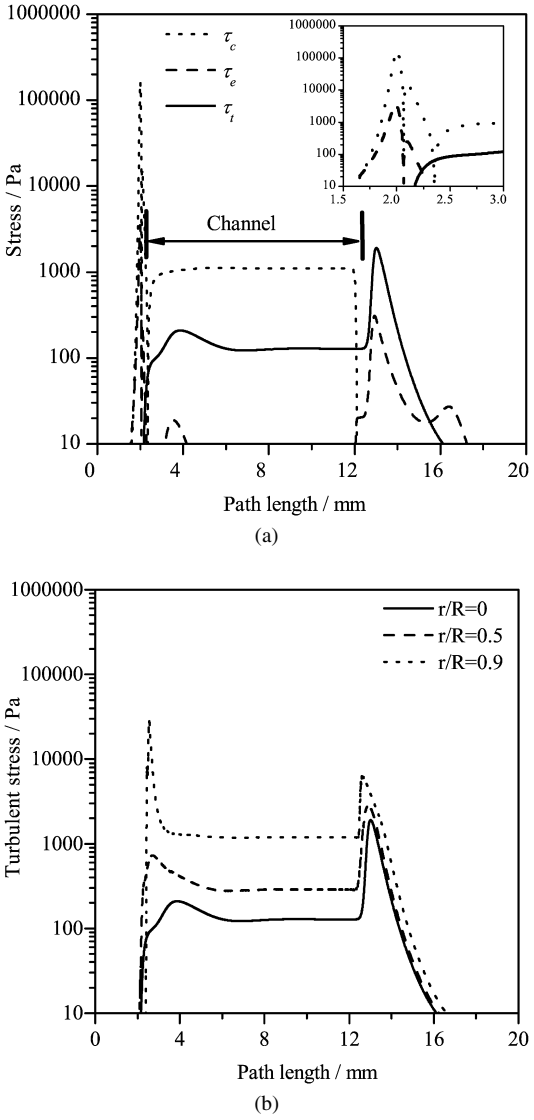

Fig. 5. Comparison compressive, elongational and turbulent stresses for $l_c = 10$ mm at Re = 30,000 for particle tracks (a) on the centerline and (b) starting from different radial positions $r/R = 0, 0.5$ and 0.9. Shear stresses are zero on the centerline. The inlet expands the channel entrance region.

a second global maximum after the channel exit in the jet region. In Fig. 5a compressive stresses dominate all others. Yet, these stresses yield a compression of the agglomerates. Therefore they do not contribute to agglomerate break-up as shown in Fig. 6, since nanoscale agglomerates withstand high compressive stresses. Additionally, elongational stresses are higher than turbulent stresses. Within the dispersion channel only turbulent and compressive stresses play a role. In the capillary the latter ones are constant at 1104 Pa. In the turbulent jet elongational and turbulent stresses decay about quadratic. This is consistent with the analytical treatment of turbulent jets presented in [16], while compressive stresses decrease rapidly.

Turbulent stresses for particles released at different radial positions (r/R) are shown in Fig. 5b. Turbulent stresses on the symmetry axis ($r/R = 0$) are lowest and increase towards the wall. Also stresses at the channel entrance become increasingly

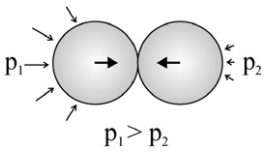

Fig. 6. Schematic representation of compressive stress due to negative pressure gradients $p_1 > p_2$. Resulting forces yield a compression of particle boding. It does not contribute to agglomerate break-up.

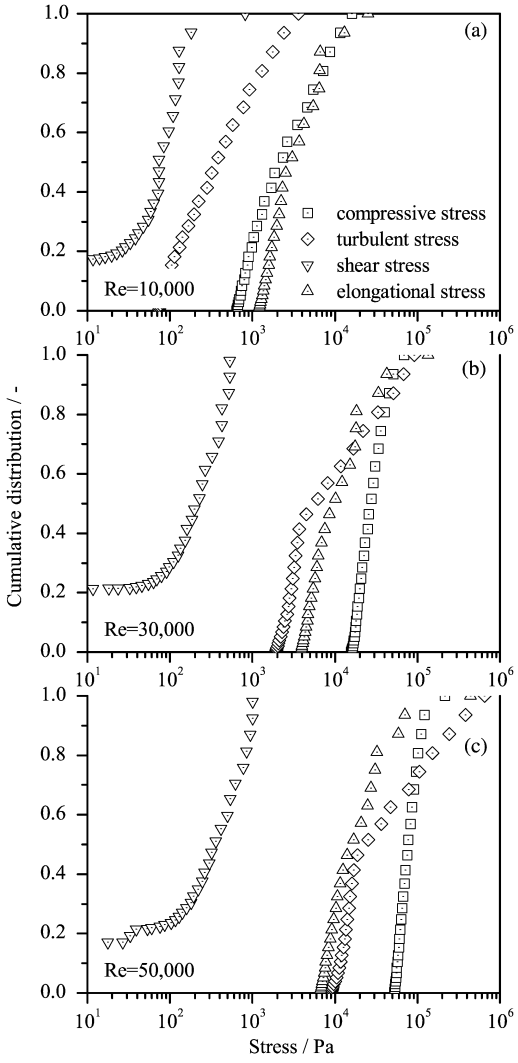

Fig. 7. Cumulative distribution of maximum stresses for particle path lines across the dispersion geometry from CFD calculations. Maximum stresses spanning more than one order of magnitude.

important toward the channel wall and are even dominating stresses in the jet at $r/R = 0.9$.

Fig. 7 shows the cumulative particle probability distribution for experiencing elongational, turbulent and compressive stresses. Assuming a constant particle concentration in the whole domain which is approximately true for low experimental particle concentrations the probability distribution of particle tracks across the capillary is given by rotational integral of a laminar flow profile with Re < 1500 at the geometry entry. Cumulative stress distributions for particle tracks are shown for Re = 10,000–50,000 (Figs. 7a–7c). At low Re elon-

gational stresses τ_e dominate for all particle tracks with stresses in the range of 10^3–10^4 Pa. Compressive stresses are slightly lower and turbulent stresses can be neglected. At Re = 30,000 all stresses are higher than at Re = 10,000 and compressive stresses τ_c dominate for ∼90% of the particles while all stresses are in the same size range for mostly stressed 10% of the particle tracks. Additionally a knee in the distribution of turbulent stresses τ_t occurs which is attributed to the influence of maximum turbulent stresses at the channel entrance dominating stresses in the turbulent jet (Fig. 7b). For 50% of the particle tracks (Re = 30,000) stresses are ordered as $\tau_c > \tau_e > \tau_t$. At Re = 50,000, elongational stresses are lowest and turbulent stresses are dominating these for all particle tracks, while compressive stresses are even higher for 75% of the particle tracks.

Assuming that highest hydrodynamic stresses determine instantaneous, nanoscale agglomerate breakage [52], since corresponding mechanical relaxation times are short, the maximum median stresses are investigated. These are exerted for at least 1 mm particle path length, which corresponds to a stressing time of about 10 µs at Re = 32,000, where this time can be considered as an upper bound for the breakage time. Fig. 8 shows numerically calculated median τ for different Re in the range of $\Delta p = 100$–1800 bar which are extracted from CFD simulations with $l_c = 10$ mm. Here different scaling laws are visible by intersection of functions. Lowest scaling is observed for shear and elongational stresses with $\tau_e \sim$ Re. Elongational stresses dominate at low Re. For compressive stresses a scaling exponent of $\tau_c \sim \mathrm{Re}^{2.2}$ is fitted numerically. Compressive stresses exceed elongational stress above Re = 12,000. Highest scaling is found for turbulent stresses with $\tau_t \sim \mathrm{Re}^{2.5}$, which theoretically exceed compressive stresses for $\mathrm{Re} > 2.5 \times 10^6$.

Compressive stresses do not contribute to agglomerate break-up. Thus different dominating stresses are found relevant for hydrodynamic dispersion in the high-pressure set-up: For Re < 12,000 ($\Delta p < 170$ bar) elongational stresses dominate, 12,000 < Re < 40,000 the fraction of particle tracks with maximum turbulent stresses is increasing and for Re > 40,000

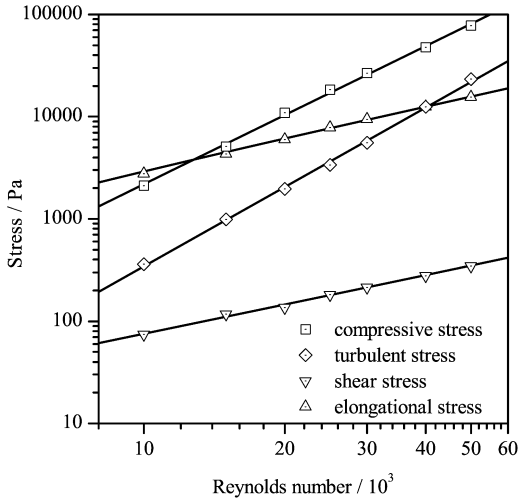

Fig. 8. Median stresses from Fig. 7 at different Re for $l_c = 10$ mm. CFD data fitted by a power law function shows good agreement with scaling exponents between 1 (shear and elongational stress) and 2.5 (turbulent stress).

($\Delta p > 1400$ bar) turbulent stresses dominate all others. Agglomerate break-up has to be attributed to a combination of elongational as well as turbulent stresses, corresponding to a turbulent shear flow [17].

5.1.3. Forces acting on aggregates in suspension

Aggregate sizes of the dispersed aggregates are in the range of 200 nm. They are in the same size range as the Kolmogorov microscale determined for the turbulent flows. Therefore it is assumed that particles do not interact with velocity fluctuations caused by fluid eddies; and particle motion can be described by viscous shear in turbulent flow. These motions are described by velocity differences (Eq. (6)) with a particle Reynolds number $\mathrm{Re_P}$ in turbulent shear flow similar to Chin et al. [20]

$$\mathrm{Re_P} = \frac{\dot{\gamma}_t \cdot d_{Agg}^2}{\nu}, \tag{20}$$

where $\mathrm{Re_P}$ ranges from 0.082 at $\Delta p = 100$ bar to 0.32 at $\Delta p = 1400$ bar for $d_{Agg} = 200$ nm. Thus viscous forces dominate inertial forces ($\mathrm{Re_P} < 1$). In Table 2 determinants of particle motion for nanoscale and macroscale particles are listed, which arise from interaction with fluid flow, particle–particle interactions and external fields. The relative importance is described by further dimensionless parameters. The ratio of inertial forces and Brownian motion is defined as Peclet number. A modified $\mathrm{Pe_P^*}$ is defined for shear flow as

$$\mathrm{Pe_P^*} = \frac{\dot{\gamma}_t \cdot d_{Agg}^2}{D} \tag{21}$$

with an aggregate diffusion coefficient $D = 2.0 \times 10^{-12}$ m^2/s for $d_P = 200$ nm. With $\mathrm{Pe_P^*}$ ranging from 4.1×10^4 to 1.6×10^5, Brownian motion is even several orders of magnitude less important than inertial forces, which have been shown to be inferior to viscous forces. Therefore Brownian motion of these aggregates can be neglected.

Besides Brownian motion and inertial forces, the influence of gravity, gravitational acceleration g, can be characterized compared to inertial forces using a Froude number [20]

$$\mathrm{Fr} = \frac{v_d^2}{d_{Agg} g} \tag{22}$$

with v_d^2 from Eq. (6), where Fr ranges from 8.57×10^4 to 1.30×10^6. The inertial forces are significantly higher than gravity and therefore gravity can be neglected also, compared to viscous and Brownian forces. These approximations show

Table 2
Determinants of particle motion for nanoscale and macroscale particles and agglomerates

	Interaction with (turbulent) fluid flow	Particle–particle interaction	External fields
Macroscale	Drag; lift, inertial forces from Reynolds stresses	Contact forces	Gravity
Nanoscale	Viscous forces from Reynolds stresses; electro-chemical double layer	Interaction potentials	Brownian motion

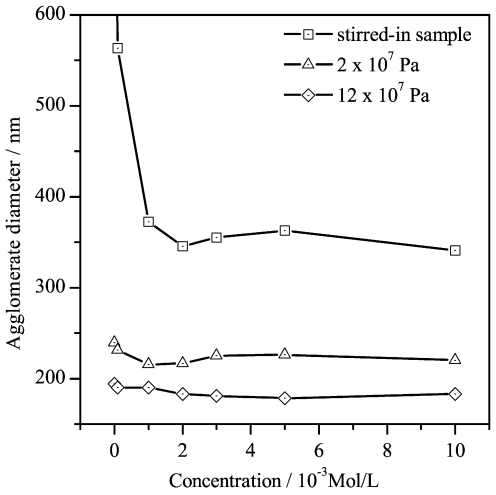

Fig. 9. Agglomerate sizes of Aerosil 200 decreases with increasing $Na_4P_2O_7$ concentration for stirred-in suspension, after high pressure dispersion at 2×10^7 and 12×10^7 Pa.

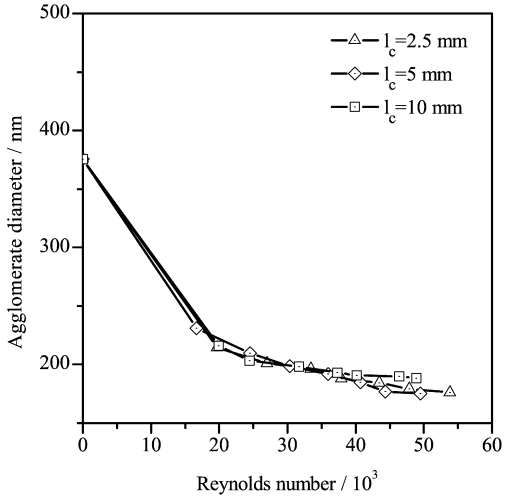

Fig. 10. Desagglomeration and aggregate fragmentation of Aerosil 200 suspensions at different channel lengths. Agglomerate diameter vs Reynolds number coincide.

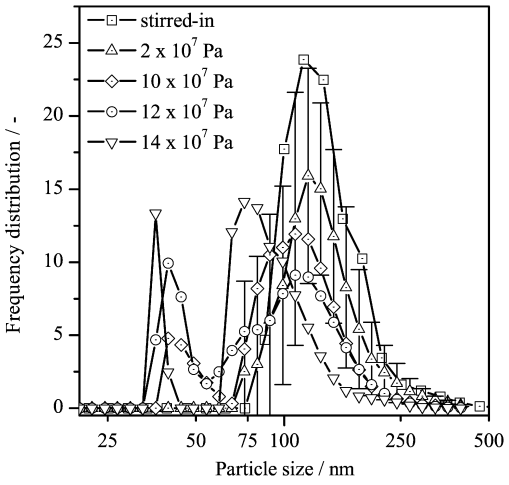

Fig. 11. Number frequency distributions of DF-silica S2 agglomerate sizes. Bimodal shape due to fragmentation indicates erosion as breakage mechanism.

the predominant influence of viscous forces on the process of nanoscale agglomerate break-up.

5.2. Experimental dispersion and fragmentation

5.2.1. Distinction between agglomerates and aggregates

Agglomerates with physically bonded primary particles and aggregates bonded by sinter necks can be distinguished by the impact of physico-chemical stabilization of the suspension. Agglomerates can be dispersed physico-chemically by adding a stabilizing agent whereas aggregates show no impact. The addition of stabilizer ($Na_4P_2O_7$) decreases the zeta-potential of these suspensions from -20 to -70 mV at concentrations of 0 and 10^{-2} mol/L. Fig. 9 shows that an increase in stabilizer concentration results in reduced agglomerate sizes for the stirred-in agglomerates due to physico-chemical dispersion.

Whereas, at $\Delta p = 200$ bar only very low stabilizer concentrations change agglomerate sizes and concentrations above 10^{-3} mol/L have no effect on the agglomerate sizes. Thus resulting aggregates are bonded by sinter necks which are not affected by stabilizing agent. The dispersion of aggregates with pressure drops of 200–1400 bar bases on fragmentation of sinter necks. Since re-agglomeration was observed neither on short nor on long term agglomeration is neglected in this study. At very low particle concentrations (0.001 v/v) as used in this work fragmentation is insensitive to concentration variations; hence fragmentation by collision can be neglected.

5.2.2. Aggregate fragmentation and morphology

Agglomerate dispersion and aggregate fragmentation was studied measuring the mean equivalent hydrodynamic diameter (DLS) at different pressure drops. Influence of morphology and size on dispersion of 'Aerosil' products and DF-silicas at different reactant flow rates has been discussed in Wengeler et al. [12]. Aggregate sizes decrease strongly from 375.4 to 215.8 nm (Aerosil 200) at low pressure drops $\Delta p < 200$ bar with only a slight reduction of 15% for $200 < \Delta p < 1400$ bar. Powders produced at low oxygen flow rates (S2) show low reduction in agglomerate size from 200 to 1400 bar with decreasing agglomerate sizes in the whole Δp range, while high oxygen flow rates (S10) yield powders with a stronger effect of pressure drop increase on agglomerate sizes where a limiting hard agglomerate size is reached at 1000 bar.

Agglomerate sizes plotted against the Reynolds number show mutual agreement of fragmentation measured at channel lengths $l_c = 2.5$, 5 and 10 mm (Fig. 10) even though corresponding pressure drops diverge (Fig. 3). This proves that fragmentation is characterized adequately by Reynolds numbers which is consistent with various studies (i.e. [29,34,53]).

The dispersion mechanism is demonstrated by the change in the number frequency distribution of agglomerate diameters from fitting the DLS-autocorrelation function of S2 particle sizing at different Δp (Fig. 11). Initially (stirred-in, squares) a unimodal distribution with a peak maximum located at 120 nm is obtained and the tail of the distribution reaches up to 1000 nm. After dispersion at 2×10^7 Pa (triangles) a bell-shaped distribution is obtained with a peak maximum at 120 nm. The

tail of the initial distribution at larger agglomerate diameters is reduced to sizes <475 nm, indicating the break-up of soft agglomerates by high pressure dispersion. As the peak of the distribution has not been shifted significantly compared to the initial distribution, this is attributed to hard agglomerates which can not be broken at this Δp. After dispersion at 10×10^7 Pa (diamonds) this mode of the distribution is still located around a peak at 120 nm, however a second peak now also appears at 45 nm. This becomes even more evident after dispersion at 14×10^7 Pa (downward triangles) where a bimodal distribution is observed with a peak of high intensity at 40 nm and a second mode at 75 nm. The agglomerate size of the first peak is comparable to the primary particle size (Table 1). This indicates that constituent primary particles erode from hard agglomerates by dispersion at 14×10^7 Pa, however a complete break-up of all hard agglomerates is not achieved. Large error bars are inherent to regularization methods for DLS [54]. Therefore size distributions are averages of three to six runs. The bimodal form has been confirmed qualitatively by TEM, by scanning mobility particle sizer measurements of dried silica nanoparticle sprays and has also been observed for dispersion of nanoscale titania [55,56].

Erosion has been observed for all DF-silica samples with bimodal size distributions comparable to Fig. 11. Yet, for strongly agglomerated powders the smaller mode does not correspond to primary particle. It can be associated to primary particle clusters [6,55] for S10 and Aerosil Ox50, which erode from aggregates due to hydrodynamic stresses. While large 'Aerosil' agglomerates as in Aerosil 200 show no bimodal size distribution and dispersion leads to a reduction of mean particle sizes of a unimodal distribution. Therefore, it is assumed that the breakage mechanism changes with increasing agglomerate sizes and aggregation numbers from primary particle erosion through cluster erosion to agglomerate break-up.

5.3. Modeling agglomerate fragmentation due to hydrodynamic stresses

5.3.1. Correlating agglomerate strength to hydrodynamic stresses

From experimental observations (Fig. 11) an erosion mechanism has been distinguished for agglomerate breakage. Normal and shear stresses on the agglomerate surface lead to particle erosion, where stresses lead to breakage of particle bonding. Since the agglomerates used in this study show low fractal dimensions of 2.15–2.2, where coordination numbers are close to two, erosion can be attributed to the breakage of a single bond.

For the fraction of dispersed primary particles, hydrodynamic stresses along agglomerate tracks have surpassed bond strength. Thus, the correlation of primary particle fraction ξ (Fig. 11) and maximum hydrodynamic stresses (Fig. 7) results in a bond strength distribution. Concerning hydrodynamic stresses a lower bound can be set by assuming that all particles eroded come from agglomerate tracks fraction Ω of minimum stress $\tau(\Omega \leqslant \xi)$. The resulting bond strength distribution of S2 (DF-silica) for median stresses and their lower bound is shown in Fig. 12. The distribution of bond strength reveals that fragmentation sets in above 5000 Pa, while final values <1 show incomplete dispersion. Here, strong sinter necks place limit to hydrodynamic stress induced dispersion. For their breakage, comminution processes need to be applied like stirred ball milling, where even primary particles can be broken and which increase the specific surface area.

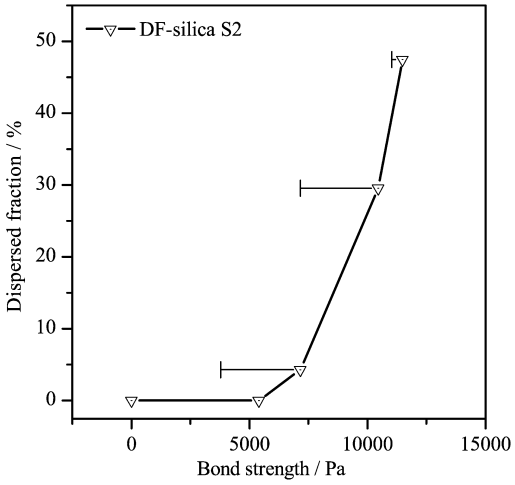

Fig. 12. Agglomerate bond strength distribution for DF-silica S2 agglomerates from fragmentation at high pressure drops of 2×10^7 to 14×10^7 Pa.

5.3.2. Scaling behavior of agglomerate fragmentation

Laminar elongational and turbulent stresses have been identified crucial for agglomerate breakage. These stresses are transduced to the agglomerates yielding breakage by agglomerate break-up and erosion. Therefore different modeling equations can be found for the different breakage regimes. Here, it is assumed that breakage occurs when hydrodynamic stresses on the agglomerates exceed their strength. This corresponds to assuming a local fragmentation number of Fa = 1 as proposed by Fanelli et al. [32]

Agglomerate breakage dominated by turbulent stresses in stirred tank reactors has been studied by [21,26]. Correspondingly, Eq. (8) is modified by embedding studies of [29,33] to result in

$$\sigma_{\mathrm{Agg,B}} = \sigma_0 \left(\frac{d_{\mathrm{Agg}}}{d_{\mathrm{P}}} \right)^{r(D_{\mathrm{f}}-3)}, \quad \text{with } \sigma_0 = \frac{F_{\mathrm{B}}}{d_{\mathrm{P}}^2}, \quad \text{for } r = 1, \tag{23}$$

which represents agglomerate break-up. While erosion is modeled by modifying Eq. (9) using the same studies to yield

$$\sigma_{\mathrm{Agg}} = \sigma_0 \left(\frac{d_{\mathrm{Agg}}}{d_{\mathrm{P}}} \right)^{r(D_{\mathrm{f}}-3)}, \quad \text{with } \sigma_0 = \frac{F_{\mathrm{B}}/d_{\mathrm{P}}}{d_{\mathrm{Agg}}}, \quad \text{for } r = 1. \tag{24}$$

Equation (18) is used to model turbulent stress while elongational stresses are modeled by Eq. (16). Assuming $\sigma_{\mathrm{Agg}} = \tau_{\mathrm{F}}$, these can be transformed to the form of Eq. (12) which result in four Eqs. (25a)–(25d) presented in Table 3.

For typical conditions in floc dispersion assuming $r = 1$ and $d_{\mathrm{f}} = 2$ Eqs. (25c) and (25d) simplify to yield scaling exponents for $\dot{\gamma}$ of $-2/3$ in case of break-up equivalent to [21] and $-1/2$ for erosion. The exponent for erosion coincides with the scaling of the Kolmogorov scale $d_{\mathrm{Agg}} \sim \varepsilon^{-0.25} \sim \eta$. Analogously,

Table 3
Model equations for agglomerate dispersion in elongational and turbulent flow assuming break-up and surface erosion mechanisms

Hydrodynamic stress	Agglomerate strength	
	Break-up $\frac{F_B}{d_P^2}\left(\frac{d_{Agg}}{d_P}\right)^{r(D_f-3)}$	Surface erosion $\frac{F_B/d_P}{d_{Agg}}\left(\frac{d_{Agg}}{d_P}\right)^{r(D_f-3)}$
Elongational stress $\nu\rho_f\dot{\gamma}_e$	$d_{Agg} = C_1^{\frac{1}{r(3-d_f)}}\dot{\gamma}_e^{-\frac{1}{r(3-d_f)}}$ with $C_1 = \frac{F_B}{d_P^2\nu\rho_f}d_P^{(3-d_f)}$, when $r=1$ (25a)	$d_{Agg} = C_2^{\frac{1}{1+r(3-d_f)}}\dot{\gamma}_e^{-\frac{1}{1+r(3-d_f)}}$ with $C_2 = \frac{F_B}{d_P\nu\rho_f}d_P^{(3-d_f)}$, when $r=1$ (25b)
Turbulent stress $\rho_l(\varepsilon\nu)^{1/2}\cdot\frac{1}{15}\left(\frac{d_{Agg}}{\eta}\right)^2$	$d_{Agg} = C_3^{\frac{1}{2+r(3-d_f)}}\dot{\gamma}_t^{-\frac{2}{2+r(3-d_f)}}$ with $C_3 = 15\frac{F_B}{d_P^2\nu\rho_f}d_P^{(3-d_f)}$, when $r=1$ (25c)	$d_{Agg} = C_4^{\frac{1}{3+r(3-d_f)}}\dot{\gamma}_t^{-\frac{2}{3+r(3-d_f)}}$ with $C_4 = 15\frac{F_B}{d_P\nu\rho_f}d_P^{(3-d_f)}$, when $r=1$ (25d)

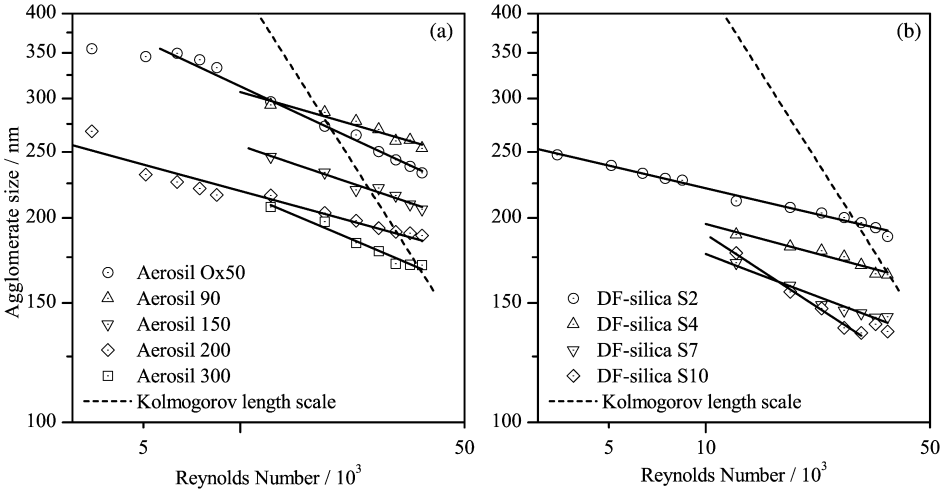

Fig. 13. Power law scaling of the dispersion process is shown for DLS agglomerates sizes for Aerosil products and DF-silicas S2–S10. Agglomerate sizes are in the range of the Kolmogorov micro scale.

the scaling exponents for elongational flow ((25a) and (25b)) in case of $r = 1$ and $d_f = 2$ are -1 for break-up and $-1/2$ for erosion.

Thus, dispersion is characterized by a power law relationship between agglomerate size and velocity gradients. Experimental data and numerical fits are shown in Figs. 13a and 13b for the 'Aerosil' and the DF-silica, respectively. The fits represent well the data set of 'Aerosil' (Fig. 13a). Comparable gradients are found for Aerosil 90, 150 to 200. While fits for Aerosil Ox50 and 300 show significantly higher gradients compared to the rest. Also, the fits for the DF-silica show a power law behavior (Fig. 13b) except for the S10 curve. Here, a limiting aggregate size is reached at Re = 25,000 which enforces separate fits for aggregate fragmentation in the range Re < 25,000 and the limiting aggregate size above. Gradients increase with aggregation number from S2 to S10 (Table 1), while decreasing d_{Agg} are attributed to fragmentation of chemical bonding [12].

As reference, Fig. 13 shows the Kolmogorov micro scale. It decreases from 356 to 130 nm at $\Delta p = 100$ and 1400 bar with higher scaling than agglomerate dispersion. The ratio d_{Agg}/η ranges from 1.5 for Aerosil 90 at Re = 50,900 to ∼0.2 at 200 bar and correspondingly low Reynolds numbers. Thus, with $d_{Agg}/\eta < 3.5$ the universal function $\beta_2 = 1/15(d_{Agg}/\eta)^2$ is valid [21] as used in Eq. (11).

Equation (12) is used to fit the experimental data using turbulent and elongational stresses from Fig. 8 to determine the velocity gradient. Table 4 shows the numerical values of the fitting parameters C and m as calculated for elongational and turbulent stresses and r is determined from m assuming both break-up and erosion mechanism. Since in the experimental range of Re < 40,000 elongational stresses dominate turbulent stresses for >50% of the particle tracks (Fig. 8), the analysis of Table 4 focuses on results for elongational stress. Turbulent fits are given for comparison.

From Aerosil 90 to 200, m increases, with $m = 0.2071$ for Ox50 being significantly higher than all others. Low scaling for Aerosil 200 shows that strong sinter necks place a limit to hydrodynamic erosion even though it has the highest aggregation number of the data set (Table 1). Whereas, within the data set 'DF-silica' m decreases from S10 to S2, attributed to decreasing Z_{Agg}. Z_{Agg} are below 10, where the primary particles size places a limit to aggregate breakage. The S10 sample shows a

Table 4
Fitting parameters (C and m) as d (nm) $= C\dot{\gamma}$ (s^{-1})^m for turbulent flow. Additionally $r(3-d_f)$ and r for break-up and erosion are calculated, with d_f measured by SAXS (Table 1). Bold values for r indicate the relevant breakage mechanism as determined from particle size distributions

Material	Turbulent stress				Elongational stress			
	C	m	$r_{\text{Break-up}}$	r_{Erosion}	C	m	$r_{\text{Break-up}}$	r_{Erosion}
Aerosil Ox50	898.50	0.0870	26.2	**25.0**	6789.9	0.2071	6.0	**4.8**
Aerosil 90	567.24	0.0510	45.4	44.2	2103.5	0.1295	9.4	8.2
Aerosil 150	512.65	0.0597	**37.5**	36.3	2332.9	0.1488	**8.0**	6.8
Aerosil 200	365.03	0.0451	**51.0**	49.8	1221.6	0.1157	**10.4**	9.2
DF-silica S2	348.40	0.0399	57.2	**56.0**	1019.9	0.1029	11.6	**10.4**
DF-silica S4	330.21	0.0467	48.0	**46.9**	1158.0	0.1194	9.9	**8.7**
DF-silica S7	362.26	0.0660	34.1	**32.9**	1988.4	0.1630	7.4	**6.2**
DF-silica S10	530.13	0.0972	18.6	**17.1**	5578.0	0.2300	6.4	**4.9**
S10 Soft	852.55	0.1366	27.3	**25.8**	15651	0.02926	5.0	**3.6**
S10 Hard	138.1	0.0004	7350	**7348.5**	154.14	0.0072	204.2	**202.8**

high $m = 0.23$ below Re = 25,000, typical for soft agglomerate breakage [26], whereas $m \to 0$ at higher Re.

The elasticity parameter r ranges from 4.8 to 10.4 (Aerosil) and from 4.9 to 10.4 (DF-silica), where bold values indicate the breakage mechanism determined from particle size distributions analysis. All r are far above unity. Thus, the differentiation of the underlying breakage process based on scaling is impossible. Therefore the mechanism from particle size distribution analysis could not be confirmed. Even $r \to \infty$ due to insensitivity of the curves towards hydrodynamic break-up, if d_{Agg} is approaching a limiting aggregate size due to strong sinter necks like 'Aerosil' products (and S10 at high Re) or primary particle size like S2. Bache [21] presents several data sets with r being in the order of unity while $r = 7.0$ for the data of [30] and $r \gg 1$ in [26]. High values of r in this study demonstrate the impact of sinter necks and correspondingly insensitivity of nanoscale material to hydrodynamic stresses.

C represents bond strength, from which the critical bond force F_B can be calculated only in case of $r = 1$ [21], which fails for the presented data. Within the data set 'Aerosil' C increases from Aerosil 200 to Ox50, while $C_2 = C^{(1/m)}$ is decreasing with correspondingly decreasing F_B. For the DF-silica, C_2 is also lessening with decreasing aggregation numbers of the powders from S10 to S2.

6. Conclusions

A high pressure dispersion device has been characterized in terms of fluid dynamics and dispersion experiments. From numerical simulations maximum stresses on agglomerates are determined on representative particle tracks, and median elongational stresses surpass turbulent stresses for Re < 40,000, while shear stresses are negligible. Highest stresses are imposed by compressive stresses; yet they do not contribute to agglomerate breakage. Typical nanoscale determinants of particle motion as Brownian forces and particle interaction potentials are negligible for stabilized suspensions.

Bond strength distributions could be determined experimentally from particle size distributions and fluid dynamics simulations. These experiments also indicate a surface erosion mechanism of agglomerate breakage for diffusion flame silica samples. This allows modeling the fragmentation process by relating agglomerate strength towards surface erosion and break-up to hydrodynamic stresses.

Nanoparticles show different dispersion properties as micron and sub-micron scale particles in flocs. Scaling of agglomerate diameter vs velocity gradient diverges from theory and shows that strong chemical bonds in nanoagglomerates opposed to attractive van der Waals forces in flocs lead to additional inelasticity. These strong sinter necks place a limit to hydrodynamic stress induced breakage. For this reason no complete dispersion of primary particles is achieved. Hence, nanoparticle properties necessitate a different design of dispersion processes.

Acknowledgments

The authors thank Prof. S.E. Pratsinis and his group, especially Ms. A. Teleki, for collaborating on pyrogenic particle synthesis and powder characterization. Financial support by the German Science Foundation (DFG; No. PAK 75/1) and by the Ministry of Science, Research and the Arts "Baden-Württemberg" is gratefully acknowledged.

References

[1] D.K. Hwang, J.H. Moon, Y.G. Shul, K.T. Jung, D.H. Kim, D.W. Lee, J. Sol–Gel Sci. Technol. 26 (2003) 783.
[2] H. Nirschl, Adv. Eng. Mater. 5 (1) (2003) 8.
[3] K. Wegner, S.E. Pratsinis, AIChE J. 49 (2003) 1667.
[4] S. Tsantilis, S.E. Pratsinis, Langmuir 20 (2004) 5933.
[5] S.E. Pratsinis, Prog. Energy Combust. Sci. 24 (1998) 197.
[6] S. Froeschke, S. Kohler, A.P. Weber, G. Kasper, J. Aerosol Sci. 34 (2003) 275.
[7] G. Kickelbick, Prog. Polym. Sci. 28 (1) (2003) 83.
[8] R.J. Nussbaumer, W.R. Caseri, P. Smith, T. Tervoort, Macromol. Mater. Eng. 288 (1) (2003) 44.
[9] F. Müller, W. Peukert, R. Polke, F. Stenger, Int. J. Miner. Process. 74S (1) (2004) S31.
[10] K.A. Kusters, S.E. Pratsinis, S.G. Thoma, G.M. Smith, Chem. Eng. Sci. 48 (24) (1993) 4119.
[11] M. Pohl, H. Schubert, H.P. Schuchmann, Chem. Ing. Tech. 77 (2005) 258.
[12] R. Wengeler, A. Teleki, M. Vetter, S.E. Pratsinis, H. Nirschl, Langmuir 22 (2006) 4928.
[13] S. Schultze, G. Wagner, J. Ullrich, Chem. Ing. Tech. 74 (2002) 901.
[14] F.A. Aguilar, B. Freudig, H.P. Schuchmann, Chem. Ing. Tech. 76 (2004) 396.

[15] N. Zumaeta, G.M. Cartland-Glover, S.P. Heffernan, E.P. Byrne, J.J. Fitzpatrick, Chem. Eng. Sci. 60 (2005) 3443.
[16] S. Pope, Turbulent Flows, Academic Press, New York, 2000.
[17] A.A. Townsend, The Structure of Turbulent Shear Flow, Cambridge Univ. Press, Cambridge, 1978.
[18] A.N. Kolmogorov, Proc. R. Soc. London A 343 (1991) 9.
[19] G.K. Batchelor, Proc. Cambridge Philos. Soc. 43 (1947) 533.
[20] C.-J. Chin, S. Yiacoumi, C. Tsouris, J. Colloid Interface Sci. 206 (1998) 532.
[21] D.H. Bache, Chem. Eng. Sci. 59 (2004) 2521.
[22] G.I. Taylor, Proc. R. Soc. A 138 (1932) 41.
[23] G.I. Taylor, Proc. R. Soc. A 146 (1934) 501.
[24] H. Nirschl, H.A. Dwyer, V. Denk, J. Fluid Mech. 283 (1995) 273.
[25] H. Rumpf, in: W.A. Knepper (Ed.), Agglomeration, Interscience, New York, 1962, p. 379.
[26] T. Neesse, K. Muehle, A. Ivanauskas, Chem. Tech. 39 (1987) 292.
[27] M. Sakurai, Y. Harano, Int. Chem. Eng. 22 (1982) 116.
[28] C.M. Sorensen, Aerosol Sci. Technol. 35 (2001) 648.
[29] R.C. Sonntag, W.B. Russell, J. Colloid Interface Sci. 115 (1987) 378.
[30] R.C. Sonntag, W.B. Russell, J. Colloid Interface Sci. 115 (1987) 390.
[31] T.M.G. Van de Ven, R.J. Hunter, Rheol. Acta 16 (1977) 534.
[32] M. Fanelli, D.L. Feke, I. Manas-Zloczower, Chem. Eng. Sci. 60 (2006) 473.
[33] A. Scurati, D.L. Feke, I. Manas-Zloczower, Chem. Eng. Sci. 60 (2005) 6564.
[34] S. Hansen, D.V. Khakhar, J.M. Ottino, Chem. Eng. Sci. 53 (1998) 1803.
[35] S.G. Mason, J. Colloid Interface Sci. 58 (1977) 275.
[36] A.A. Potanin, J. Colloid Interface Sci. 157 (1993) 399.
[37] K. Higashitani, K. Iimura, H. Sanda, Chem. Eng. Sci. 56 (2001) 2927.
[38] D.S. Parker, W.J. Kaufmann, J. Jenkins, J. Sanitary Eng. Div. 98 (1972) 79.
[39] B.E. Launder, D.B. Spalding, Comput. Meth. Appl. Mech. Eng. 3 (1974) 269.
[40] T.-H. Shih, W.W. Liou, A. Shabbir, Z. Yang, J. Zhu, Comp. Fluids 24 (3) (1995) 227.
[41] T. Narayanan, O. Diat, P. Boesecke, Nucl. Instrum. Methods Phys. Res. Sect. A 467 (2001) 1005.
[42] S.W. Provencher, Comput. Phys. Commun. 27 (1982) 229.
[43] G. Beaucage, H.K. Kammler, S.E. Pratsinis, J. Appl. Crystallogr. 37 (2004) 523.
[44] D.A. Weitz, J.S. Huang, M.Y. Lin, J. Sung, Phys. Rev. Lett. 54 (1985) 1416.
[45] P. Meakin, Phys. Rev. Lett. 51 (1983) 1119.
[46] R. Wengeler, H. Nirschl, in: U. Teipel (Ed.), Fraunhofer, IRB-Verlag, Stuttgart, 2006.
[47] M. Soos, J. Sefcik, M. Morbidelli, Chem. Eng. Sci. 61 (2006) 2349.
[48] S. Harada, R. Tanaka, H. Nogami, N. Sawada, J. Colloid Interface Sci. 301 (2006) 123.
[49] W.M. Kays, Trans. ASME 72 (1950) 1067.
[50] A.K.M.F. Hussain, V. Ramjee, Trans. ASME (1976) 58.
[51] C.T. Crowe, M. Sommerfeld, Y. Tsuji, Multiphase Flows with Droplets and Particles, CRC Press, Boca Raton, 1998.
[52] R.C. Sonntag, W.B. Russell, J. Colloid Interface Sci. 113 (1986) 399.
[53] P. Jarvis, B. Jefferson, J. Gregory, S.A. Parsons, Water Res. 39 (2005) 3121.
[54] A. Moeller, Deutsche Nationalbibliothek; http://deposit.ddb.de, Darmstadt 2000.
[55] N. Mandzy, E. Grulke, T. Druffel, Powder Technol. 160 (2005) 121.
[56] Y.-J. Lee, D.L. Feke, I. Manas-Zloczower, Chem. Eng. Sci. 48 (19) (1993) 3363.